Chinese Chemical Letters 37 (2026) 111985

Contents lists available at ScienceDirect

Chinese Chemical Letters

journal homepage: www.elsevier.com/locate/cclet

Synergistic photocatalysis and biochemical reactivity in MXene/CuO_2 nanofibrous membrane for enhanced sterilization and tissue regeneration in chronic skin wounds

Mingxiao Liu[a,1], Wenzhuo Zheng[a,1], Jianru Yi[a], Jiahe Li[a], Jiyao Li[a], Yi Deng[c], Fusong Yuan[b,*], Kunneng Liang[a,*], Zhihe Zhao[a,*]

[a] State Key Laboratory of Oral Diseases, National Center for Stomatology, National Clinical Research Center for Oral Diseases, Sichuan University, Chengdu 610041, China
[b] Center of Digital Dentistry/Department of Prosthodontics, National Clinical Research Center for Oral Diseases, Peking University School and Hospital of Stomatology, Beijing 100081, China
[c] School of Chemical Engineering, Sichuan University, Chengdu 610041, China

ARTICLE INFO

Article history:
Received 9 June 2025
Revised 16 October 2025
Accepted 20 October 2025
Available online 21 October 2025

Keywords:
Bio-heterojunctions
Phototherapy
Synergistically antibacterial
Angiogenesis
Wound healing

ABSTRACT

Chronic skin wounds with persistent bacterial infections present a formidable clinical challenge, characterized by recurrent infections and delayed healing. These issues stem from incomplete bacterial eradication, a lack of sustained antibacterial ability, and slow tissue repair. We developed a dual-responsive nanocatalytic membrane to address these limitations for advanced infected chronic wound management. This platform integrates MXene/CuO_2 bio-heterojunctions (MX/CO bio-HJs) with polydopamine (PDA) and electrospun polycaprolactone (PCL) scaffolds, creating a multifunctional system that synergistically enhances debridement and regeneration. Diverging from traditional dressings, this membrane leverages near-infrared (NIR) light to trigger robust antibacterial action through synergistic photodynamic (PDT) and photothermal (PTT) therapies, ensuring complete sterilization. In the absence of NIR, it autonomously responds to the infection microenvironments (IMEs) by initiating Fenton-like cascades *via* chemodynamic therapy (CDT) and metal-ion therapy (MIT), sustaining reactive oxygen species (ROS) production and Cu^{2+} ions release to prevent recurrent infections. Simultaneously, the released Cu^{2+} ions enhance vascular endothelial growth factor (VEGF) expression, fostering angiogenesis and hastening wound closure, thus reducing infection risks linked to prolonged exposure. *In vivo* studies demonstrate rapid bacterial elimination, significant remodeling of the wound milieu, and enhanced epithelialization, collagen deposition, and vascularization. This innovative design overcomes the deficiencies of existing modalities, offering a NIR/IMEs dual-responsive approach to managing chronic infected wounds with precision and efficacy.

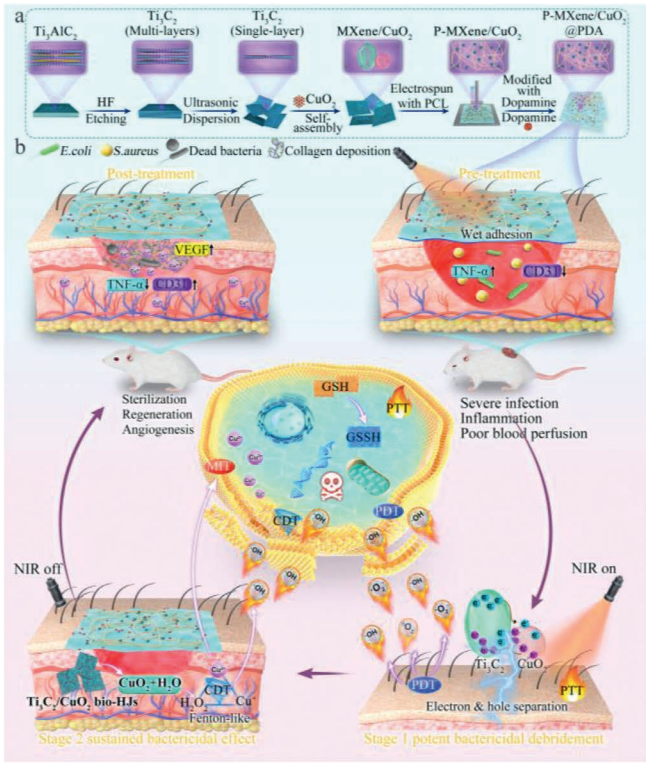
© 2026 Published by Elsevier B.V. on behalf of Chinese Chemical Society and Institute of Materia Medica, Chinese Academy of Medical Sciences.

The epidermis, the body's most extensive organ, serves as the frontline defense and is crucial for sustaining systemic balance and protecting internal tissues from external hazards [1]. Upon cutaneous injury, a dynamic repair cascade unfolds, progressing through four interdependent phases: hemostasis, inflammation, proliferation, and remodeling [2,3]. This intricate process relies on the coordinated interplay between immune cells, fibroblasts, and other cellular constituents to restore barrier integrity [4]. However, chronic skin wounds disrupt this orchestration, presenting a complex pathophysiological milieu that conventional therapies such as standard dressings, hyperbaric oxygen, and antibiotics struggle to address effectively [5–8]. Although antibiotics are pivotal in controlling infections, their systemic toxicity and the rapid spread of resistant pathogens intensify challenges for global healthcare [9–12]. Consequently, a multifunctional antibiotic-free platform that ensures sustained antimicrobial activity while promoting tissue repair is critical.

For debridement of chronic infected skin wounds, phototherapy has become a paradigm-shifting strategy for combating wound infections [13–16]. Photothermal therapy (PTT) exploits light-induced hyperthermia to destabilize bacterial membranes, while photodynamic therapy (PDT) unleashes a reactive oxygen species (ROS) cascade to amplify bactericidal potency [17–21]. Despite its potential, conventional phototherapy fails to resolve chronic wounds owing to three critical limitations: Under light activation, the insuffi-

* Corresponding authors.
E-mail addresses: yuanfusong@bjmu.edu.cn (F. Yuan), kunnengliang@scu.edu.cn (K. Liang), zhzhao@scu.edu.cn (Z. Zhao).
[1] These authors contributed equally to this work.

https://doi.org/10.1016/j.cclet.2025.111985
1001-8417/© 2026 Published by Elsevier B.V. on behalf of Chinese Chemical Society and Institute of Materia Medica, Chinese Academy of Medical Sciences.



Scheme 1. (a) Fabrication process for P-MCP nanofibrous membrane *via* sequential assembly and functionalization. (b) *In vivo* application of P-MCP membrane demonstrating antimicrobial efficacy and skin regeneration in an infected wound mouse model.

cient synergy between PDT and PTT leads to incomplete bacterial clearance [18]; once light ceases, the inherent light-dependency of photodynamic approaches creates vulnerability to secondary infections during dark intervals [22]. Prolonged bacterial exposure triggers persistent inflammatory responses and delayed vascularization [23,24]. Therefore, there is a great need to develop novel phototherapy biomaterials to treat chronic wounds.

In this study, we developed a dual-responsive platform that harnesses the synergistic interplay of PTT and PDT within MXene/CuO_2 bio-heterojunctions (MX/CO bio-HJs), as displayed in Scheme 1. This p-n heterojunction establishes a built-in electric field that enhances charge separation and migration, amplifies photocatalytic efficiency, and has great potential to sustain antibacterial ability even without external light [25–28]. First, under near-infrared (NIR) light activation, MX/CO bio-HJs drive potent hyperthermia *via* PTT, disrupting bacterial membranes [29]. At the same time, CuO_2 generates a ROS storm through PDT, collectively ensuring comprehensive pathogen elimination [29,30]. Second, under dark conditions within exudative infection microenvironments (IMEs), CuO_2 nanoparticles (NPs) in MX/CO bio-HJs react with wound exudate-derived water to generate hydrogen peroxide (H_2O_2), a key substrate driving Fenton-like cascades [31,32]. This reaction triggers chemodynamic therapy (CDT), unleashing the ROS barrage to eradicate residual bacteria. This process sustains a dynamic Cu^{2+}/Cu^{+} redox cycle, ensuring continuous ROS generation post-illumination. Complementing CDT, the Cu^{2+} ions liberated during metal ion therapy (MIT), exerting intrinsic bactericidal effects by compromising membrane integrity, inactivating proteins, and damaging DNA. This CDT-MIT strategy establishes a persistent antimicrobial shield that effectively mitigates the risk of secondary infections when the light is withdrawn. Moreover, the released Cu^{2+} ions liberated during CDT and MIT bolster infection control and serve as bioactive cues, stimulating fibroblast proliferation and upregulating vascular endothelial growth factor (VEGF) expression [33]. This dual functionality accelerates angiogenesis and enhances vascularization, the key drivers of granulation tissue formation and epithelialization. The platform minimizes the temporal window of vulnerability to reinfection by expediting wound closure, directly addressing the risks posed by prolonged lesion exposure.

For optimal wound healing, we embedded MX/CO bio-HJs within electrospun polycaprolactone (PCL) fibrous membranes designed to mimic the extracellular matrix (ECM) with their nanoscale architecture and high surface area-to-volume ratio [17,34]. Inspired by mussel adhesion chemistry, we functionalized these scaffolds with a polydopamine (PDA) coating, conferring robust wound bed adhesion even in exudative IMEs. This adhesion arises from the synergy of covalent (Michael addition and Schiff base formation) and non-covalent (hydrogen bonding, electrostatic) interactions, establishing a durable, conformal barrier that maintains intimate contact with the wound surface [20,35,36].

In summary, we propose an innovative NIR/IMEs dual-responsive P-MXene/CuO_2@PDA (P-MCP) nanocatalytic membrane that can manage persistent infected wounds by simultaneously tackling sterilization and tissue repair. Under NIR irradiation, this platform exhibits synergistic PTT and PDT effects, amplifying its antimicrobial potency. Intriguingly, incorporating CuO_2 NPs sustains H_2O_2 production, thereby driving Fenton-like reactions and enabling controlled Cu^{2+} ion release. These features ensure that the IMEs-triggered CDT and MIT can be sustained without light. Beyond infection control, liberated Cu^{2+} ions further stimulate angiogenesis, accelerate vascularization, and promote wound healing. By thoughtfully integrating MX/CO bio-HJs, PDA, and PCL, this design provides a multifaceted therapeutic approach that addresses the dual challenges of chronic bacterial infections and impaired tissue regeneration, which could markedly improve clinical outcomes.

To validate our experimental design, we synthesized and characterized the novel MX/CO bio-HJs system for enhanced infected wound healing (Scheme 1a). Monolayer MXene (Ti_3C_2) nanosheets were synthesized *via* solution-phase exfoliation by etching Ti_3AlC_2 in lithium fluoride/hydrochloric acid, followed by ultrasonication. CuO_2 NPs were intercalated into the MXene framework through electrostatic self-assembly. As shown in Fig. S1 (Supporting information), scanning electron microscopy (SEM) revealed Ti_3AlC_2 with accordion-like multilayer nanostructures, while delaminated MXene nanosheets (Fig. S1a) showed uniform distribution confirmed by transmission electron microscope (TEM) (Fig. S1b). Upon assembly, CuO_2 NPs exhibited reduced size and uniform distribution across the MXene surface due to negatively charged functional groups regulating crystallization (Fig. 1a). TEM showed intimate MXene/CuO_2 bonding (Fig. 1e), while high-resolution TEM (HRTEM) revealed distinct lattice intersections confirming heterojunction formation (Fig. 1b). Lattice parameters showed interplanar spacings of 0.245 and 0.26 nm, corresponding to CuO_2 (111) and MXene (010) planes, respectively. Atomic force microscope (AFM) indicated ~20.2 nm height for monolayer MXene, consistent with theoretical values (Fig. 1d) [37]. Energy-dispersive X-ray spectroscopy (EDS) mapping demonstrated homogeneous Cu, O, Ti, and C distributions, validating successful bio-HJ construction (Fig. 1f). X-ray diffraction (XRD) (Fig. 1i) and Fourier-transform infrared spectroscopy (FTIR) (Fig. S1e) confirmed composition and chemical bonding. XRD revealed unchanged CuO_2 peaks after assembly, preserving catalytic properties. FTIR demonstrated MXene's characteristic Ti-O-C vibration at 618 cm^{-1}, validating successful MX/CO bio-HJs construction and stability.

Building upon the successful synthesis of MX/CO bio-HJs, we next fabricated the electrospun nanocatalytic membrane to serve as a multifunctional platform that localizes catalytic activity and avoids systemic dissemination of non-degradable elements. These ECM-mimicking membranes with nanometer to micrometer fiber

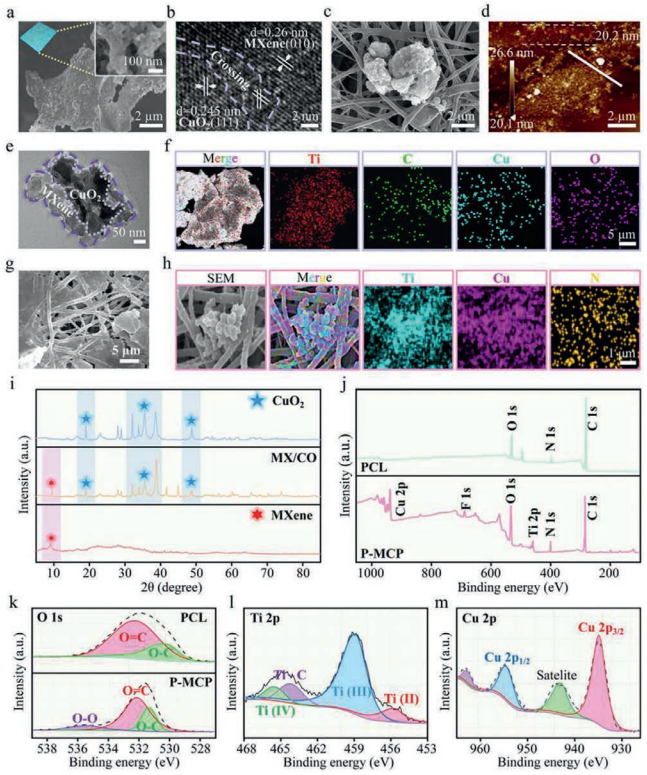


Fig. 1. Heterojunction and membrane characterization: (a) SEM image of MX/CO bio-HJs (inset: pure CuO_2 NPs). (b) HRTEM and (c) SEM images of P-MX/CO. (d) AFM and (e) TEM images of MX/CO bio-HJs. (f) Elemental mapping of MX/CO bio-HJs. (g) SEM images and (h) elemental mapping of P-MCP. (i) XRD patterns of MXene, MX/CO bio-HJs, and CuO_2 NPs. (j) XPS survey spectra of pristine PCL and P-MCP. (k–m) High-resolution XPS spectra: O 1s, Ti 2p, and Cu 2p.

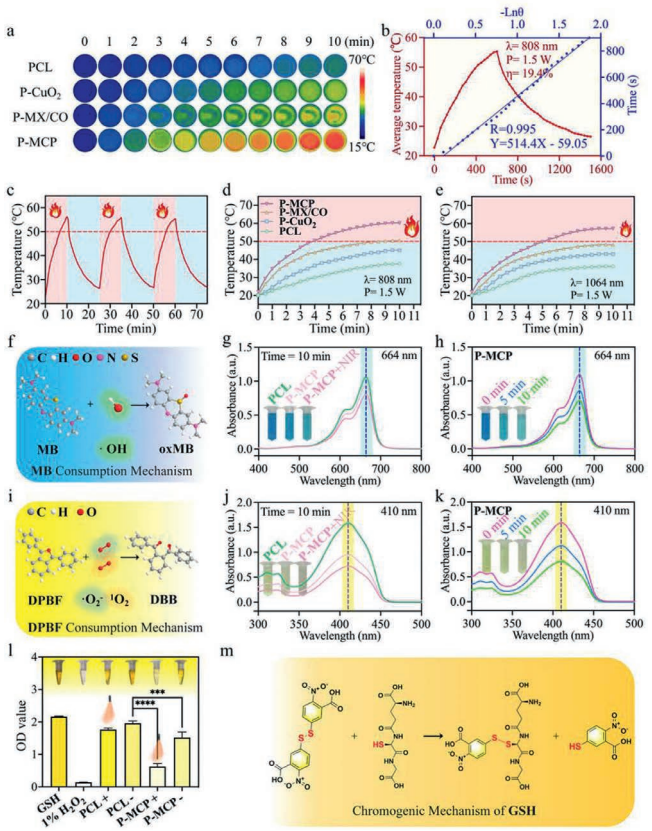


Fig. 2. Evaluation of the photothermal and photocatalytic performance of the membrane: (a) Real-time infrared thermal images of different groups. (b) Photothermal response of P-MCP over 600 s under NIR laser irradiation (808 nm, 1.5 W/cm^2), followed by laser shutdown, with a linear time plot *versus* Lnθ. (c) Photothermal stability was assessed using three on/off irradiation cycles. Photothermal heating curves of the electrospun membrane under (d) 808 nm and (e) 1064 nm laser irradiation. (f) Schematic representation illustrates the mechanism. (g, h) Spectral analysis of MB degradation. (i) Conceptual illustration and (j, k) absorption spectra of DPBF depletion. (l) GSH depletion and (m) its underlying mechanism. Data are presented as mean ± standard deviation (SD) ($n = 3$).

diameters are ideal for wound dressings. SEM revealed pristine PCL membranes with uniform nanofibers and 1–2 μm interfibrous pores optimal for cellular attachment (Fig. S1c). P-CuO_2 and P-MX/CO membranes showed successful integration of MX/CO bio-HJs and CuO_2 NPs on fiber surfaces (Fig. 1c and Fig. S1d), while PDA-modified membranes exhibited distinctive film-like coatings (Fig. 1g). EDS mapping confirmed spatial distribution of Ti and Cu from MX/CO bio-HJs and N from PDA coating (Fig. 1h). X-ray photoelectron spectroscopy (XPS) analysis confirmed successful MX/CO bio-HJs incorporation into the PCL matrix. The survey spectrum showed characteristic peaks at Cu 2p (935 eV), F 1s (687 eV), O 1s (532 eV), Ti 2p (459 eV), N 1s (400 eV), and C 1s (285 eV), with no Al signals indicating complete Ti_3AlC_2 etching (Fig. 1j). P-MCP showed additional Ti 2p, F 1s, and Cu 2p peaks compared to pristine PCL. O 1s deconvolution revealed peaks at 535.58 eV (O–O), 532.98 eV (C–O), and 531.78 eV (C=O), with O–O bonds confirming MX/CO bio-HJs incorporation (Fig. 1k). Ti 2p spectra showed peaks at 465.68 eV (Ti IV), 464.38 eV (Ti-C), 458.98 eV (Ti III), and 455.88 eV (Ti II), with predominant Ti(III) indicating substantial MXene presence (Fig. 1l). Cu 2p spectrum displayed peaks at 954.78 eV (Cu $2p_{1/2}$) and 934.88 eV (Cu $2p_{3/2}$) with corresponding satellite peaks (Fig. 1m).

To further characterize the membrane's suitability for wound applications, we evaluated its physical and biological properties. Detailed adhesion strength measurements at various tensile angles, surface wettability analysis, and biocompatibility evaluation using L929 and HaCaT cell lines are provided in the Supporting Information (Figs. S2 and S4 in Supporting information).

With the membrane's structural integrity confirmed, we subsequently evaluated its photothermal properties using a FLIR E6 thermal camera to assess NIR-mediated heat generation. P-MCP exhibited superior photothermal performance (Fig. 2a), with MX/CO bio-HJs and PDA integration enhancing 808 nm NIR-to-thermal energy conversion. Under 808 nm NIR irradiation (1.5 W, 500 s), P-MCP reached a maximum temperature of 55.3 °C, followed by rapid cooling post-irradiation (Fig. 2b). The photothermal conversion efficiency was 19.4 %, confirming P-MCP's suitability for NIR-mediated therapies. P-MCP maintained excellent stability over ten heating-cooling cycles with minimal temperature variation (Fig. 2c). Under dual-wavelength irradiation (808/1064 nm) at varying power densities (Figs. 2d and e), P-MCP outperformed P-CuO_2 and P-MX/CO in PBS, reaching 60.2 °C under 808 nm due to PDA's efficient NIR conversion, while P-MX/CO reached 50.5 °C in 10 min, driven by enhanced electron-hole separation at the MX/CO bio-HJs interface. PCL showed minimal thermal response.

Complementing the photothermal evaluation, we assessed the photocatalytic ROS generation of P-MCP, starting with ·OH production using methylene blue (MB) as a probe, which exhibited reduced absorption at 664 nm upon reaction (Fig. 2f) [38]. P-MCP+NIR exhibited significantly lower MB absorbance than P-MCP alone, while PCL showed negligible changes (Fig. 2g). Enhanced ·OH production stemmed from MX/CO bio-HJs' PDT effect and CuO_2 NPs' H_2O_2 generation for Fenton-like reactions. Time-dependent MB absorbance decreased under 808 nm irradiation, indicating sustained photocatalytic activity (Fig. 2h). Singlet oxy-

gen ($^1O_2$) and superoxide ($^{\bullet}O_2^-$) generation were assessed using 3-diphenylisobenzofuran (DPBF), with a characteristic absorbance drop at 410 nm (Fig. 2i) [39]. P-MX/CO showed superior ROS generation compared to PCL, attributed to efficient electron-hole separation at the MXene-CuO_2 heterojunction interface (Fig. 2j). NIR irradiation further reduced DPBF absorbance over time, confirming sustained ROS production (Fig. 2k). Glutathione (GSH) depletion, a key bacterial defense against oxidative stress [40], was significantly enhanced by P-MCP under dark and NIR conditions, with P-MCP+NIR showing the highest depletion rate after the 1.0% H_2O_2 control (Figs. 2l and m). P-MCP maintained substantial GSH consumption without NIR, indicating CuO_2's independent catalytic activity. PCL and PCL+NIR showed negligible GSH depletion. These results highlight MX/CO bio-HJs and PDA integration's ability to disrupt bacterial GSH defenses, with enhanced efficacy under NIR irradiation.

Leveraging these demonstrated photothermal and photocatalytic capabilities, we next evaluated the *in vitro* antibacterial efficacy against Gram-positive (*S. aureus*, ATCC 25,923) and Gram-negative (*Escherichia coli*, ATCC 25,922) strains using spread plate assays, SEM, and TEM [41,42]. As shown in Fig. 3 and Fig. S3 (Supporting information), PCL exhibited minimal antibacterial activity against both strains regardless of NIR irradiation (Figs. 3a and b, Figs. S3a and b). The P-CuO_2, P-MX/CO, and P-MCP groups demonstrated enhanced antimicrobial properties with corresponding decreases in bacterial survival rates (Fig. 3c and Fig. S3c). P-MCP achieved >30% antimicrobial efficiency without NIR irradiation, attributed to MIT effects from Cu^{2+} ions and CDT-generated ROS from IME stimulation. Despite 10.0 min NIR irradiation, substantial bacterial colonies persisted in P-CuO_2+NIR (survival rates: 85.53% ± 4.14% for *E. coli*, 95.9% ± 1.92% for *S. aureus*), demonstrating PTT's limited standalone antimicrobial capacity. The P-MX/CO+NIR group showed significantly reduced bacterial survival (7.77% ± 3.72% for *E. coli*, 8.83% ± 1.27% for *S. aureus*) due to bio-HJs optimizing charge carrier dynamics and enhancing photogenerated electron-hole pair separation. Most impressively, P-MCP+NIR exhibited dramatic bactericidal effects with survival rates of only 0.47% ± 0.34% (*E. coli*) and 0.87% ± 1.02% (*S. aureus*) through synergistic photothermal heating, ROS production, and Cu^{2+} release. SEM analysis (Fig. 3d and Fig. S3d) and TEM examination (Fig. 3e) revealed morphological changes and membrane integrity alterations. PCL groups maintained characteristic bacterial morphologies with intact structures. P-CuO_2 groups showed minimal changes with surface wrinkles. P-MX/CO and P-MCP groups, particularly under NIR irradiation, induced significant morphological damage including membrane wrinkles, contraction, and dehiscence. P-MCP+NIR caused the most severe damage: Disrupted cell walls and cytoplasmic membranes, cytoplasmic leakage, vesicular intracellular density transformation, invisible DNA, and *E. coli* flagella detachment. The P-MCP bactericidal mechanism follows multiple pathways (Scheme 1b): CuO_2 NPs react with H_2O to produce H_2O_2, which generates ROS *via* Fenton-like reactions with Cu^{2+} ions (CDT). Under NIR irradiation, MX/CO bio-HJs initiate dual-mode action through PTT and PDT. Photothermal conversion increases local temperature for thermal ablation while accelerating CDT [43]. The resulting ROS storm causes oxidative damage through lipid peroxidation, protein denaturation, and nucleic acid fragmentation while oxidizing GSH to glutathione disulfide (GSSH), disrupting bacterial antioxidant defenses [44,45]. During MIT, released Cu^{2+} ions accumulate on bacterial membranes, bind phospholipids, increase permeability, and cause cellular content leakage [46].

In parallel with its antimicrobial effects, we investigated the membrane's ability to promote angiogenesis using a Matrigel-based tube formation assay with human umbilical vein endothelial cell (HUVEC). Fig. 3f and Fig. S3e show HUVEC tube formation progression on various substrates at 5 and 15 h time points, selected to capture initial tube formation dynamics and mature tubular networks before apoptosis onset. This dual approach comprehensively characterizes both initiation and stabilization phases of angiogenesis. While all groups supported angiogenic activity, P-MCP demonstrated the most extensive capillary-like structure development, quantitatively confirmed in Fig. 3j and Fig. S3f with statistically significant increases in tubule formations. Fluorescence microscopy (Fig. 3g and Fig. S3g) and quantitative analyses (Figs. 3h and i, Figs. S3h and i) revealed marked VEGF upregulation in the P-MCP group. Strong green fluorescence in VEGF immunostaining correlated with enhanced angiogenic activity compared to controls. Three-dimensional z-axis intensity plots (Fig. 3g and Fig. S3g) confirmed spatial distribution patterns, with P-MCP-treated cells exhibiting peak VEGF expression. These findings indicate P-MCP supports both structural capillary formation and angiogenic signaling upregulation, consistent with literature demonstrating Cu^{2+} ions stimulate VEGF-mediated angiogenic processes and vascular structure stabilization [33,47]. P-MCP membranes exhibited distinctive Cu^{2+} release kinetics: Rapid NIR-triggered liberation followed by

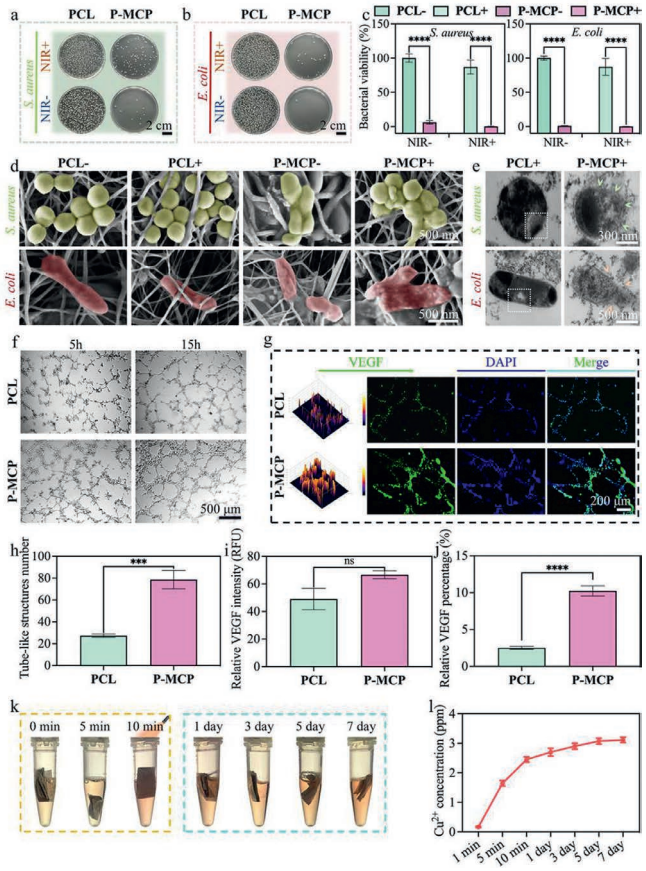


Fig. 3. NIR-enhanced antibacterial activity and angiogenic promotion by P-MCP: Images of *S. aureus* (a) and *E. coli* (b) colonies following P-MCP treatment. (c) Quantitative bacterial viability for *S. aureus* and *E. coli*. (d) SEM images showing morphological changes in *S. aureus* and *E. coli* cultured with different P-MCP components ± NIR irradiation. (e) TEM images of ultrastructural changes in bacteria treated with PCL+NIR or P-MCP+NIR. White dotted boxes indicate heat-induced membrane damage; arrows denote membrane damage with cytoplasmic leakage. (f) HUVEC tube-like structures in Matrigel assay following P-MCP treatment. (g) 3D reconstructions of HUVEC tube-like structures labeled with VEGF and DAPI. VEGF fluorescence relative proportion (h) and signal intensity (i) quantifying angiogenic responses. (j) Quantitative analysis of HUVEC tube-like structures at 15 h. (k) Cu^{2+} ion release profile from P-MCP. Deeper red represents higher Cu^{2+} concentration. (l) Cu^{2+} concentration visualization in each time point. Data presented as mean ± SD ($n = 3$).

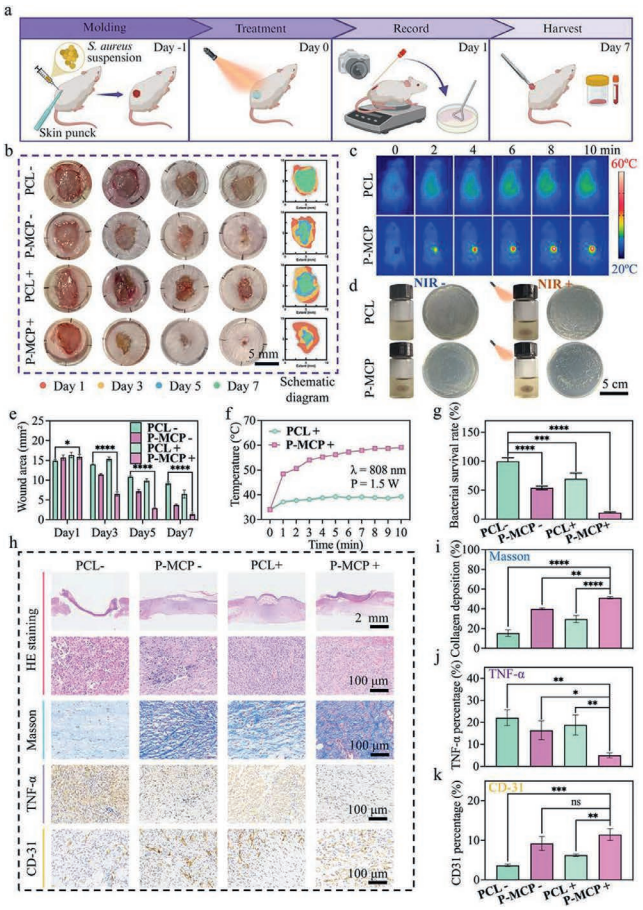


Fig. 4. *In vivo* assessment of bacterial eradication and wound healing: (a) Schematic of animal experimental procedures. (b) Sequential photographs of treated skin wounds from day 1 to day 7. (c) Thermal imaging of wounds under NIR irradiation. (d) Turbid liquid and *S. aureus* colonies from infected wounds post-treatment. (e) Quantitative wound healing area analysis. (f) Surface temperature of membranes under NIR irradiation. (g) Bacterial viability rates measured by CFUs on day 1. (h) H&E, Masson's trichrome, TNF-α and CD31 staining of skin tissues following treatments. Quantitative analysis of (i) collagen volume fraction from Masson's trichrome staining, (j) TNF-α levels, and (k) CD31 levels. Data presented as mean ± SD ($n = 3$).

sustained dark-condition release (Figs. 3k and l). During initial NIR activation, Cu^{2+} concentrations reached 2.45 ± 0.09 μmol/L within 10 min (~80% of total release), then increased gradually from 2.70 ± 0.13 μmol/L (day 1) to equilibrium at 3.11 ± 0.09 μmol/L (day 7). This release mechanism originates from CuO_2 NP hydrolysis, generating Cu^{2+} ions and H_2O_2 in the wound-mimicking environment. NIR irradiation enables MX/CO bio-HJs to convert light into localized heat, enhancing hydrolysis rates and amplifying initial Cu^{2+} burst. Post-NIR exposure, hydrolysis continues at physiological conditions with steady Cu^{2+} accumulation reflecting ongoing CuO_2 dissolution.

Having confirmed robust *in vitro* performance in both sterilization and angiogenesis, we next validated the P-MCP membrane's therapeutic efficacy *in vivo* using a full-thickness infected skin defect model in Kunming mice (Fig. 4a). All animal experiments were approved by the West China Hospital of Stomatology's Animal Care Committee (No. WCHSIRB-D-2018–089) and conducted in compliance with NIH guidelines for animal welfare. Treatment groups included NIR-irradiated (P-MCP+NIR/PCL+NIR) and non-irradiated (P-MCP-NIR/PCL-NIR) conditions. Mice initially lost weight during the first three days but gradually recovered as treatment progressed (Fig. S5a in Supporting information). P-MCP+NIR-treated wounds exhibited accelerated closure compared to other groups (Fig. 4b). While no significant differences were observed initially, by day 7 this group demonstrated the most pronounced size reduction with nearly complete epithelialization (Fig. 4e). Thermographic analysis on day 1 (Figs. 4c and f) showed PCL+NIR maintained ~38.15 °C with no significant temperature change due to inability to convert light energy to heat. P-MCP+NIR exhibited rapid temperature increase from 34.0 °C to 59.0 °C within 10.0 min, confirming substantial *in vivo* photothermal conversion consistent with *in vitro* results. Antibacterial assessment using wound-derived bacteria (day 1) showed P-MCP+NIR demonstrated the lowest bacterial turbidity, fewest colonies, and highest antimicrobial rate (88.79%, Figs. 4d and g). Healing efficiency was significantly higher in P-MCP+NIR *vs.* P-MCP-NIR, attributed to synergistic antimicrobial effects of PTT and PDT. Even without NIR, P-MCP-NIR showed better healing outcomes than both PCL groups due to CDT, MIT, and Cu^{2+}-mediated angiogenic effects. The PCL+NIR group outperformed PCL-NIR, likely due to NIR irradiation promoting local blood circulation despite PCL's lack of therapeutic properties.

To gain deeper insights into the observed *in vivo* healing, we performed comprehensive histological analyses of wound tissues. Hematoxylin and eosin (H&E) staining on day 7 (Fig. 4h) revealed minimal neutrophil infiltration in the P-MCP+NIR group, indicating largely resolved inflammation. Significant inflammation persisted in PCL-NIR, PCL+NIR, and P-MCP-NIR groups, with abundant neutrophils observed in both PCL groups. The PCL+NIR group showed initial epithelial ingrowth without complete coverage, while PCL-NIR exhibited minimal epithelial regeneration. The P-MCP-NIR group demonstrated fewer neutrophils, more mature granulation tissue, increased vascular and fibroblast presence, and improved epithelial regeneration, indicating progression to tissue remodeling. The P-MCP+NIR group exhibited the fewest neutrophils, fully mature granulation tissue, uniform vessel and fibroblast distribution, and new connective tissue formation with continuous, well-defined epithelial layers of significantly increased thickness. Masson staining confirmed collagen deposition patterns (Fig. 4h). By day 7, comparable collagen fiber levels were observed in PCL-NIR, PCL+NIR, and P-MCP-NIR groups. P-MCP+NIR displayed significantly more intense collagen staining (51.18% ± 1.16%) and higher density of newly formed blood vessels with red cells between collagen fibers (Fig. 4i). P-MCP-NIR promoted repair even under dark conditions (collagen percentage: 39.96% ± 0.72%), while NIR application synergistically shortened inflammation and accelerated collagen deposition and angiogenesis. Immunohistochemistry evaluated inflammatory response and antibacterial efficacy using CD31 (platelet-endothelial marker) and tumor necrosis factor-alpha (TNF-α) [13,48,49]. TNF-α showed significantly higher positive areas in PCL groups, indicating severe inflammation (Fig. 4j). TNF-α expression was markedly reduced in P-MCP groups, with lowest levels in P-MCP+NIR (5.02% ± 0.92%), resulting from synergistic bacterial elimination that removed the primary inflammatory stimulus. CD31 was upregulated in P-MCP groups (Fig. 4k), with significant increases in new capillaries observed in P-MCP+NIR (11.45% ± 1.22%). This enhanced CD31 expression stems from P-MCP's antibacterial capabilities mitigating inflammation and Cu^{2+} ions promoting angiogenesis [50,51].

As shown in Fig. S5, body weight measurements showed transient decline during initial two days with no subsequent fluctuations, suggesting no long-term adverse effects (Fig. S5a). Routine hematological assessments revealed no significant abnormalities, confirming systemic safety (Fig. S5b). H&E staining of major organs (heart, liver, spleen, lungs, kidneys) showed minimal adverse effects, underscoring P-MCP's great biocompatibility (Fig. S5c).

In summary, we have engineered an innovative NIR/IMEs dual-responsive nanocatalytic membrane that effectively combines swift bacterial elimination with enhanced healing of infected skin

wounds. Under NIR excitation, the MX/CO bio-HJs induce photogenerated electron and hole separation, exerting a potent synergistic PTT and PDT bactericidal effect. The modification of PDA can not only make the electrospun membrane tightly bind to the skin wound through the formation of chemical bonds and non-covalent interactions under wet conditions, but also enhance the photothermal conversion efficiency of PTT. Remarkably, even after NIR withdrawal, the P-MCP membrane reacts with water in the IME to supply endogenous H_2O_2. The MX/CO bio-HJs, with their excellent Fenton-like reactivity, catalyze the conversion of H_2O_2 into abundant ROS *via* the Cu(I)/Cu(II) redox cycle, resulting in a robust CDT bactericidal effect. Furthermore, the generated ROS oxidizes GSH to GSSH, compromising the antioxidant defense function of bacteria. The release of Cu^{2+} ions during this process provides a sustained MIT bactericidal and pro-angiogenic effect, accompanied by the activation of VEGF. This nanocatalytic membrane exhibited high bactericidal potency both *in vitro* and *in vivo* through a quintuple synergistic approach involving CDT, PTT, PDT, MIT, and GSH depletion, demonstrating excellent photothermal conversion efficiency, ROS generation, and antibacterial activity under NIR light. Furthermore, P-MCP membranes demonstrated excellent biocompatibility, and *in vivo* studies confirmed their ability to accelerate wound healing by modulating the pathological chronic microenvironment into a regenerative state. This transformation enhanced collagen deposition, stimulated angiogenesis, and mitigated inflammatory responses. The experimental outcomes provide valuable insights for designing NIR/IMEs dual-responsive nanofiber membranes, offering a promising strategy for managing infected skin wounds. The innovative approach harnessing the synergistic effects of multiple therapeutic modalities, combined with the responsive nature of the nanocatalytic membrane, offers a promising strategy for addressing the challenges associated with chronic wound healing.

CRediT authorship contribution statement

Mingxiao Liu: Writing – review & editing, Writing – original draft, Validation, Formal analysis, Data curation, Conceptualization. **Wenzhuo Zheng:** Writing – review & editing, Writing – original draft, Validation, Formal analysis, Data curation, Conceptualization. **Jianru Yi:** Validation, Supervision, Methodology. **Jiahe Li:** Writing – original draft, Validation, Data curation. **Jiyao Li:** Validation, Supervision, Methodology. **Yi Deng:** Writing – review & editing, Supervision, Resources, Project administration, Funding acquisition, Conceptualization. **Fusong Yuan:** Validation, Supervision, Funding acquisition, Conceptualization. **Kunneng Liang:** Writing – review & editing, Supervision, Resources, Project administration, Funding acquisition, Conceptualization. **Zhihe Zhao:** Validation, Supervision, Funding acquisition, Conceptualization.

Declaration of competing interest

The authors declare that they have no known competing financial interests or personal relationships that could have appeared to influence the work reported in this paper.

Acknowledgments

This work was supported by National Natural Science Foundation of China (Nos. 82270970, 82470967, 32271416), International Orthodontics Foundation Young Grant Award (No. IOF2022Y04) and Natural Science Foundation of Sichuan Province (No. 2025ZNSFSC1591). We gratefully acknowledge BioRender for the creation of the feature icons used in Fig. 4a and Fig. S5c, which greatly enhanced the visual representation of our research.

Supplementary materials

Supplementary material associated with this article can be found, in the online version, at doi:10.1016/j.cclet.2025.111985.

References

[1] S. Salman, V. Paulet, K. Hardonnière, S. Kerdine-Römer, BioFactors 51 (2025) e70013.
[2] J.Y. Ding, M.J. Chen, L.F. Wu, et al., Mil. Med. Res. 10 (2023) 36.
[3] R. Song, H. Xie, G. Liu, Chin. Chem. Lett. 36 (2025) 110442.
[4] P. Martin, C. Pardo-Pastor, R.G. Jenkins, J. Rosenblatt, Science 386 (2024) eadp2974.
[5] F. Yousefian, R. Hesari, T. Jensen, et al., Antibiotics 12 (2023) 1434.
[6] L. Long, W. Liu, C. Hu, L. Yang, Y. Wang, Biomater. Sci. 10 (2022) 4058–4076.
[7] Y. Xu, L. Ma, Y. Wang, C. Shi, Chin. Chem. Lett. 36 (2025) 109766.
[8] Q. Yang, X. Sun, Q. Ding, et al., Natl. Sci. Rev. 11 (2024) nwae225.
[9] C. Mao, Y. Xiang, X. Liu, et al., ACS Nano 12 (2018) 1747–1759.
[10] Y. Yamazaki, T. Ito, M. Tamai, S. Nakagawa, Y. Nakamura, Inflamm. Regen. 44 (2024) 9.
[11] L. Huelsboemer, L. Knoedler, A. Kochen, et al., Mil. Med. Res. 11 (2024) 23.
[12] D. Prakashan, A. Kaushik, S. Gandhi, Chem. Eng. J. 497 (2024) 154371.
[13] C. Xu, J. Li, C. Ou, et al., Chem. Eng. J. 499 (2024) 156170.
[14] S. Iravani, R.S. Varma, RSC Adv. 13 (2023) 9665–9677.
[15] M. Li, Y. Yang, J. Gong, et al., Nano Lett. 24 (2024) 16208–16219.
[16] R. Zhang, Y. Zhou, S. Gao, J. Zhang, Chin. Chem. Lett. 36 (2025) 110829.
[17] Q. Yu, C. Wang, X. Zhang, et al., ACS Nano 18 (2024) 14085–14122.
[18] A. Naskar, K.S. Kim, Pharmaceutics 15 (2023) 1116.
[19] L. Lei, W. Dai, J. Man, et al., J. Nanobiotechnology 21 (2023) 482.
[20] S. Cheng, M. Pan, D. Hu, et al., Chin. Chem. Lett. 34 (2023) 108276.
[21] M. Qi, Q. Ding, Y. Shi, et al., Biomaterials 324 (2026) 123487.
[22] Y. Feng, C. Coradi Tonon, S. Ashraf, T. Hasan, Adv. Drug Deliv. Rev. 177 (2021) 113941.
[23] F. Sozmen, M. Kucukoflaz, M. Ergul, Z.D. Sahin Inan, RSC Adv. 11 (2021) 2383–2389.
[24] Y. Zhao, J. Liu, L. Sun, et al., J. Nanobiotechnology 23 (2025) 424.
[25] K.A. Papadopoulou, A. Chroneos, D. Parfitt, S.R.G. Christopoulos, J. Appl. Phys. 128 (2020) 170902.
[26] H. Liu, X. Zhu, R. Han, et al., New J. Chem. 44 (2020) 1795–1805.
[27] Q. Chi, G. Zhu, D. Jia, et al., Nanoscale 13 (2021) 4496–4504.
[28] A. Balapure, J. Ray Dutta, R. Ganesan, RSC Appl. Interfaces 1 (2024) 43–69.
[29] S. Li, Q. Ding, L. Zhang, et al., J. Control. Release 370 (2024) 600–613.
[30] X. Sun, J. Sun, Y. Sun, et al., Adv. Funct. Mater. 31 (2021) 2101040.
[31] R. Zhang, G. Jiang, Q. Gao, et al., Nanoscale 13 (2021) 15937–15951.
[32] X. Wang, C. Ding, Z. Zhang, et al., Chin. Chem. Lett. 34 (2023) 107951.
[33] B. Li, W. Yang, R. Shu, et al., Adv. Mater. 36 (2024) e2307613.
[34] B. Joseph, R. Augustine, N. Kalarikkal, et al., Mater. Today Commun. 19 (2019) 319–335.
[35] C. Zhang, L. Xiang, J. Zhang, et al., Chem. Sci. 13 (2022) 1698–1705.
[36] N. Li, X. Ji, S. Mukherjee, et al., ACS Appl. Mater. Interfaces 15 (2023) 10383–10397.
[37] W. Dai, R. Shu, F. Yang, et al., Adv. Mater. 36 (2024) e2305277.
[38] Y. Ran, M. Moursy, R.C. Hider, A. Cilibrizzi, Int. J. Mol. Sci. 24 (2023) 4162.
[39] Z. Wang, B. Du, X. Gao, et al., Nano Today 46 (2022) 101595.
[40] H.J. Forman, H. Zhang, Nat. Rev. Drug Discov. 20 (2021) 689–709.
[41] J. Li, L. Zhou, M. Liu, X. He, T. Huang, Tissue Eng. Part C: Methods 31 (2025) 230–236.
[42] J. Li, M. Fan, Z. Jiao, et al., Nano Today 59 (2024) 102541.
[43] J. Huo, Q. Jia, H. Huang, et al., Chem. Soc. Rev. 50 (2021) 8762–8789.
[44] Y. Wang, J. Xiong, L. Xin, et al., Chin. Chem. Lett. 36 (2025) 110003.
[45] J. Guo, Y. Lin, S. He, et al., Chin. Chem. Lett. 35 (2024) 109537.
[46] I. Salah, I.P. Parkin, E. Allan, RSC Adv. 11 (2021) 18179–18186.
[47] S. Lee, S.M. Lee, S.H. Lee, et al., Acta Biomater. 172 (2023) 159–174.
[48] R. Shu, J. Sun, B. Li, et al., Adv. Funct. Mater. 33 (2023) 2214873.
[49] J. Wang, Z. Gao, H. Liang, et al., Chin. Chem. Lett. 36 (2025) 110569.
[50] M. Tian, Z. Li, S. Liu, et al., Chem. Eng. J. 491 (2024) 152130.
[51] L. Chen, J. Min, F. Wang, Signal Transduct. Target. Ther. 7 (2022) 378.